Vector Acoustic Analysis of Time-Separated Modal Arrivals From Explosive Sound Sources During the 2017 Seabed Characterization Experiment

Peter H. Dahl ⬤, *Senior Member, IEEE*, and David R. Dall'Osto

Abstract—The Intensity Vector Autonomous Recorder (IVAR) is a system that records four coherent channels of acoustic data continuously: one channel for acoustic pressure and three channels associated with a triaxial accelerometer from which acoustic particle velocity is obtained. IVAR recorded the vector acoustic field in broadband signals originating from Signal, Underwater Sound (SUS) (Mk-64) charges deployed at 5–13-km range from the fixed IVAR site (mean depth 74.4 m) as part of the 2017 Seabed Characterization Experiment (SBCEX) designed to study the acoustics of fine-grained muddy sediments. Sufficient geometric dispersion at these ranges permitted unambiguous identification of up to four modes as a function of frequency for frequencies less than 80 Hz. From time–frequency analysis of the dispersed arrivals, a single mode (n) and single-frequency (f_i) properties are identified at peaks in the narrowband scalar field, with time dependence corresponding to mode group speed. At these time–frequency addresses, four quantities derived from the vector acoustic measurements are formed by coherent combination of pressure and velocity channels: first, modal phase speed; second, circularity, a measure of the normalized curl of active intensity; third, depth-dependent mode speed of energy; and fourth, vertical component of reactive intensity normalized by scalar intensity. A means to compute these quantities theoretically is provided, and a comparison of model results based on a notional geoacoustic representation for the SBCEX experimental area consisting of a single low-speed mud layer over a half-space area versus a Pekeris representation based on the same half-space shows a striking difference, with the field observations also clearly at variance with the Pekeris representation. A fundamental property of mode 2, observed at the IVAR location, is a change in sign for circularity and vertical reactive intensity near 37 Hz that is posited as a constraint observation for mode 2 that must be exhibited by any geoacoustic model that includes a low-speed mudlike layer applied to this location.

Index Terms—Acoustic particle velocity, active intensity, circularity, group speed, modal speed of energy, phase speed, reactive intensity, vector acoustics.

P. H. Dahl is with the Applied Physics Laboratory and the Department of Mechanical Engineering, University of Washington, Seattle, WA 98105 USA (e-mail: dahl@apl.washington.edu).
D. R. Dall'Osto is with the Applied Physics Laboratory, University of Washington, Seattle, WA 98105 USA (e-mail: dallosto@apl.washington.edu).

I. INTRODUCTION

THE Intensity Vector Autonomous Recorder (IVAR) is a system that records four coherent channels of acoustic data continuously: one channel for acoustic pressure and three channels associated with a triaxial accelerometer from which acoustic particle velocity is obtained. IVAR was deployed on the seafloor during the Seabed Characterization Experiment (SBCEX), conducted 95 km south of Martha's Vineyard, MA, USA, in 2017. The primary goal of the SBCEX is to study the acoustics of fine-grained muddy sediments that are a prominent feature of the experimental area. For example, the upper most sediment layer commencing at the water–sediment interface is known to consist of fine-grained mudlike material [1] with geoacoustic properties largely unknown before the SBCEX [2].

The IVAR was deployed on the seafloor from *R/V Endeavor* during the SBCEX for two periods: 7 March 1645Z to 9 March 1415Z (45.5 h) and 17 March 2330Z to 18 March 2030Z (22 h). During both deployments, the IVAR recorded signals (frequency range 50–500 Hz) from a towed source (J-15) deployed from *R/V Endeavor*, the noise field from large cargo vessels operating nearby, and signals from the various experimental sound sources used by other investigators during the SBCEX.

During the second deployment, the IVAR recorded arrivals from broadband SUS (Mk-64) charges deployed from *R/V Neil Armstrong*. The focus of this study is on the IVAR observations of SUS deployments at ranges 5–13 km from the fixed IVAR location. At these ranges and in view of the ∼74-m depth, there is sufficient geometric dispersion of the broadband explosive SUS pulse to allow identification of four distinct modes below 80 Hz.

This work does not engage in a geoacoustic inversion of field results *per se*; instead it presents a purely observational description of four quantities derived from the vector acoustic measurements that are sensitive to modal properties as realized at the IVAR site. These quantities are formed by the coherent combination of pressure and particle velocity and are as follows:

1) modal phase speed;
2) circularity, a measure of the normalized curl of active intensity;
3) depth-dependent mode speed of energy;
4) the vertical component of reactive intensity normalized by scalar intensity.
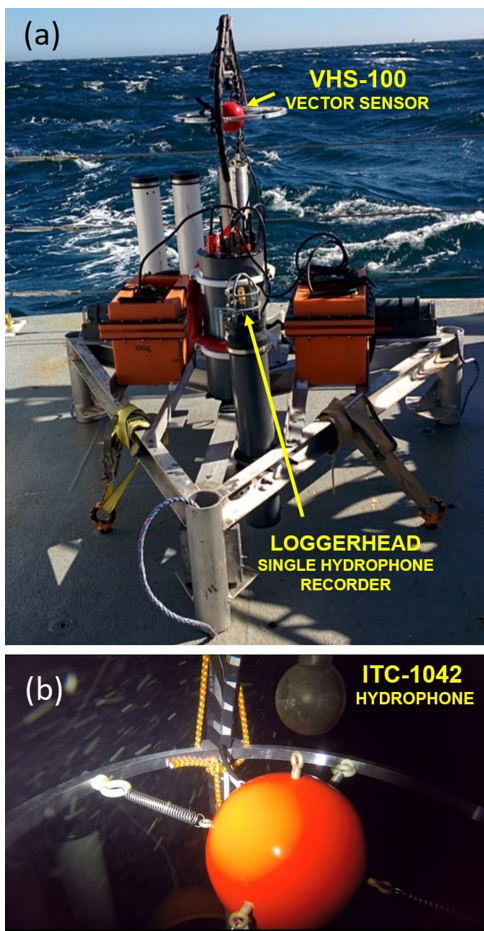
Fig. 1.   Annotated photographs of IVAR (a) on aft deck of *R/V Endeavor* and (b) as deployed on seafloor. Streaks are marine snow carried by the ocean current.

To guide interpretation and provide a pathway to exploit these properties in geoacoustic inversion, a method to compute these quantities theoretically using a normal mode-based propagation code is also provided, and we present computed forms associated with a notional geoacoustic model. For example, we will demonstrate an important property of mode 2 as it goes through a transition in the neighborhood of 37 Hz; the existence of this transition and its location in frequency appears to be strongly dependent on the surficial low-speed mud layer at the IVAR site.

This paper is arranged as follows: in Section II, the IVAR system is described with key details relating to its second deployment and measurement of SUS charges. Section III describes the data processing, first covering broadband vector intensity for context, and then addressing the narrowband processing more closely associated with this study. In Section IV, the vector acoustic quantities for single-mode single frequency are formally defined along with corresponding models, and field results are presented in Section V. A summary and some additional remarks are provided in Section VI.

II. IVAR System and Deployment During SBCEX

The IVAR system consists of a bottom-deployed tripod [see Fig. 1(a)] where key components include a three-axis accelerometer contained within a 10-cm diameter neutrally buoyant sphere

(VHS-100, Ocean Applied Acoustics) and an omnidirectional hydrophone (ITC-1042) positioned 10 cm above the center of the sphere. The accelerometer and hydrophone are coherently recorded (25 000-Hz sample rate), in four low-gain (0 dB) and four high-gain (30 dB) channels. Key metadata including water depth and sensor orientation were recorded every 15 s over the duration of the deployment. Because it was important to verify proper suspension of the neutrally buoyant sphere, a video record was taken for each deployment to document the descent phase of IVAR and first few minutes on the seafloor [see Fig. 1(b)]. Note that a second single-hydrophone recording system (Loggerhead Instruments, Inc., Sarasota, FL, USA) is also mounted on the IVAR to provide a back-up set of hydrophone data although this data stream is not recorded coherently with accelerometer data.[1]

Combining co-located and coherently measured particle velocity with pressure provides a direct measure of vector intensity. Particle velocity as measured over three axes is obtained, depending on processing application, by either time integration or frequency division of the acceleration channels. With radius $a = 5$ cm and k equal to acoustic wave number based on sound speed in water, the neutrally buoyant sphere responds sufficiently similar to an accelerating parcel of water for frequencies up to about $ka \sim 0.8$, or 3750 Hz [3], although we limit our study to frequencies less than 1000 Hz to avoid any need for vertical phase corrections between pressure and particle velocity. Measurements at higher frequencies are still possible but ultimately the integrated pressure distribution over the surface of the sphere divided by mass of water displaced will not equate to acoustic particle acceleration for an equivalent volume of water.

At low frequencies, all channels are limited by the highpass filtering (-3 dB corner frequency equal to 25 Hz).[2] Owing to the roll-off in particle acceleration with frequency, reliable particle velocity estimates at 25 Hz require signal levels greater than about 120 dB re 1 μ Pa, whereas the pressure channel could detect somewhat lower levels.

For the second deployment, the IVAR was placed at location 49.48655 °N, −70.63831 °W where mean water depth was 74.4 m varying by ±0.4 m owing to the M2 tidal variation [see Fig. 2(a)]. A CTD cast taken from *R/V Endeavor* [see Fig. 2(b)] shortly before recovery of IVAR shows a relatively well-mixed water column typical of other observations made during SBCEX [4]. In our subsequent manipulation of vector acoustic data, we implement the depth average as representing an isovelocity water column, with sound speed $c_w = 1468.3$ m/s.

The broadband source was the Mk-64 SUS charge consisting of 31 g of tetryl designed to detonate at notional depth of 18.3 m. These sources were deployed from *R/V Neil Armstrong* at locations (SUS stations) planned and coordinated by P. Wilson and D. Knobles and a separate study related to these sources is in preparation. At each station, a sequence of five SUS charges

---

[1]Some researchers in SBCEX are utilizing this hydrophone data for purposes of geoacoustic inversion.

[2]In hindsight, this was an overly conservative setting meant to protect the channels from possible saturation from very nearby sources. For future studies, we have set a lower corner frequency to 8 Hz.
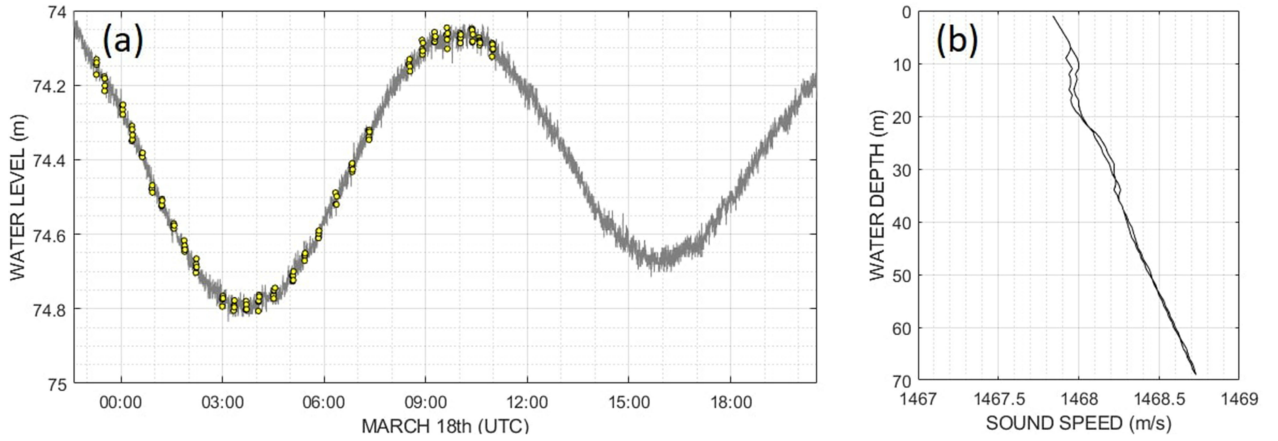
Fig. 2. (a) Water level measured by a depth sensor on the IVAR tripod, time of SUS charges indicated by circles. (b) Sound speed versus depth made by conductivity–temperature–depth (CTD) cast from *R/V Endeavor*; average speed equals 1468.3 m/s.
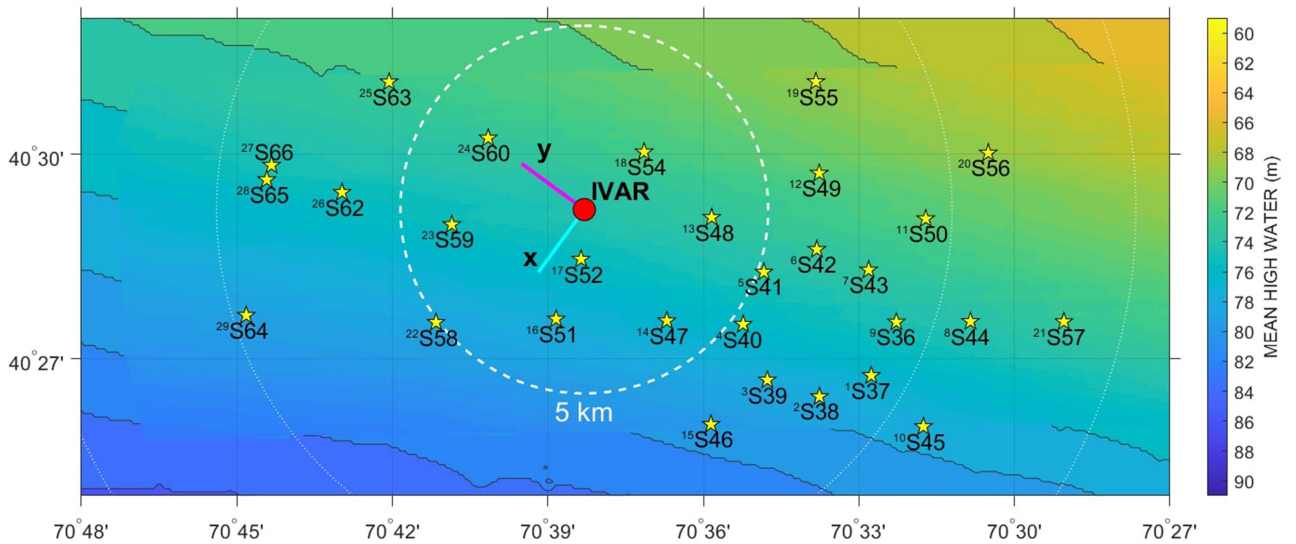

Fig. 3. Distribution of Mk-64 SUS detonation stations (stars) observed by the IVAR system (red circle); orientation of *x*-axis (cyan) and *y*-axis (magenta) indicated. Analysis is based on 22 stations outside the dashed circle delineating range 5 km from the IVAR. Note that each SUS detonation station presents a unique orientation with respect to the *x* and *y* axes of the IVAR system, e.g., the response from station S40 is manifested primarily on the *y*-axis.

were deployed separated in time by approximately 20 s. The second deployment of the IVAR coincided with a subset of SUS deployments, a total of 29 stations for which the range between SUS detonation (*R/V Neil Armstrong*) and IVAR location on the seabed varied between 3 and 13 km (see Fig. 3). However, to realize sufficient geometric dispersion, we limit this analysis to the 22 stations that fall outside the dashed circle in Fig. 3. The center of the neutrally buoyant sphere on the IVAR was positioned 1.25 m above the seafloor, with the *x*-axis aligned with true bearing 216.3° and *y*-axis aligned with 306.3°. For example, the bearings to stations S40 and S45 (see Fig. 3) are aligned with the *y*-axis.

III. CALCULATING ACOUSTIC ENERGY DENSITY AND VECTOR INTENSITY

A. Broadband Vector Intensity

In the following, broadband pressure $P(t)$ and components of particle velocity $V_{x,y,z}(t)$, over the bandwidth 10–1000 Hz,

are discussed briefly where the latter are obtained by time integration of the measured acceleration time series (although levels for frequencies less than 25 Hz are reduced somewhat owing to the aforementioned highpass filtering.) Results from a single detonation (see Fig. 4) from SUS station S40, range 5 km, shows the broadband, potential energy density $(1/2)|P(t)|^2/(\rho c_w^2)$ and kinetic energy density $(1/2)\rho|V(t)|^2$, as each varies over time. These are based on water density, ρ equal to 1027.6 kg/m³, and c_w equal to 1468.3 m/s. The relative time reference is set by the arrival of the peak waterborne path, and a time average over relative time period 0–0.5 s brings the two energy densities to within 0.14 dB (the 0.5-s time averaging period encompassing 99% of the energy.)

The segment of data commencing ∼450 ms before arrival of the peak waterborne path (relative time equal to 0) suggests the onset of a ground wave [5] associated with the emergence of mode 2 at frequency ∼22 Hz. This frequency inferred from the pattern in Fig. 4 made clear in this decibel view, with 22 Hz being too high for the cutoff of mode 1 given the water depth. Note
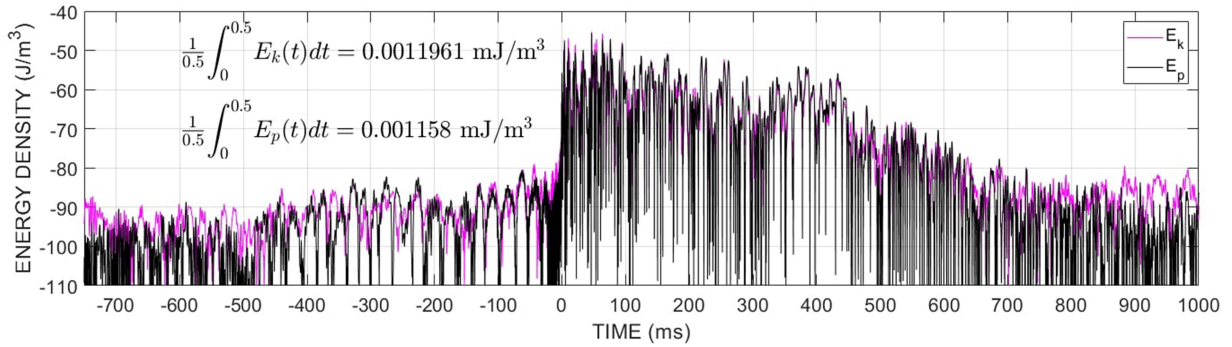
Fig. 4.   Time-varying potential (black) and kinetic (magenta) energy densities measured at the IVAR site from a SUS arrival originating at station S40, range 5 km. Time is relative to the arrival of the peak waterborne path.

that the mode 2 precursor is evident in the kinetic energy density but somewhat more poorly resolved by the velocity channels because of the highpass filtering mentioned in Section II. Similarly, the relatively narrowband region (frequency ∼28 Hz) centered about 400 ms after arrival of the peak waterborne path is likely associated with the Airy phase for mode 2; this frequency being more readily inferred from the same pattern upon expanding the scale. The received waveform embodies the expected bubble pulse [6] of period ∼42 ms as can be confirmed with autocorrelation. The bubble pulse can produce the interference that is observed primarily at frequencies greater than about 500 Hz, at frequency intervals ∼24 Hz. However, the bubble pulse effect is not problematic for this analysis and we make no further attempt to remove it.

Shown on a linear scale are corresponding broadband pressure (see Fig. 5, top row) and components of particle velocity (see Fig. 5, middle row), where owing to the alignment of the y-axis of the vector sensor with source direction of SUS station S40, the y-component dominates over the x-component. The Umov vector $S_{x,y,z}(t)$ or instantaneous intensity (see Fig. 5, bottom row) is formed by multiplying $P(t)$ by separate components of particle velocity.

The time average of the components of the broadband Umov vector over the same 0–0.5 s period yields estimates of the active intensity vector, with values for the separate components identified. Note that the value of the y-component of active intensity is close to an equivalent time average of $(P(t)^2/\rho c_w)$, or scalar intensity, a result anticipated given that the y-component of particle velocity normalized by ρc_w approximately equals the pressure for this case that is the representative of a single active source with dominant energy flux in the horizontal direction. The z-component of the broadband Umov vector varies between negative and positive values; this change in direction of the sound field flow is indicative of reactive intensity [7], as defined and discussed in Section III-B. There exists a small nonzero time average in the positive z (downward) direction, and we observe the broadband vertical flux to be in general 0.03–0.04 times the corresponding horizontal flux for the 22 stations (see Fig. 3) studied.

In the remainder of this study, we examine properties associated with both active and reactive intensities in greater detail as function of mode and frequency, made possible by the geometric dispersion of the SUS arrivals for ranges greater than about

5 km. The frequency range studied will necessarily be limited to <80 Hz, where there is sufficient time separation among modes. New notation for complex narrowband pressure and particle velocity is necessary along with model counterparts as a function of mode and frequency. We avoid reusing $P(t)$ and $V_{x,y,z}(t)$, reserving these for real broadband quantities.

B. Time–Frequency Analysis

Time–frequency analysis is done with a bank of bandpass filters applied to the original data in the time domain (using the low-gain set of channels in all cases), each with bandwidth B equal to 4 Hz centered at frequencies between 10 and 80 Hz, every 1 Hz. We use this approach rather than, say, an equivalent one involving short-time Fourier transforms, as our preference is to use intensity units over spectral densities.

An analytic signal is formed from the measured narrowband filtered time series for pressure $p_{M_i}(t)$, centered at f_i, by constructing a Hilbert-transformed pair $p_i(t) = p_{M_i}(t) + i\hat{p}_{M_i}(t)$, where $\hat{p}_{M_i}(t)$ is the Hilbert transform of the signal that is 90° out of phase with $p_{M_i}(t)$. The analytic signal $p_i(t)$ is henceforth used as a complex representation of the pressure data. Potential energy density $E_{p_i}(t)$ (J/m^3) as a function of time and centered at f_i is thus

$$E_{p_i}(t) = \frac{1}{4}|p_i(t)|^2/(\rho c^2). \tag{1}$$

An image of $E_{p_i}(t)$ [see Fig. 6(a)] for one of the five SUS detonations at station S45 (range 10 km) shows the arrival separated into the first four modes. Results from the other four detonations from S45 are similar. We can easily identify the maximum value of $E_{p_i}(t)$ for each mode and frequency, the time–frequency locations for which are identified by the dots in Fig. 6(a). These time–frequency addresses are an important part of our analysis to identify modes as a function of frequency.

Time series for the three components of complex velocity, as in the x-component v_{x_i} centered at f_i are calculated by dividing the complex representation of the corresponding measured and narrowband filtered acceleration channel a_{x_i} by $-i2\pi f_i$, where a_{x_i} also represents a Hilbert-transformed pair. The kinetic energy density $E_{k_i}(t)$ is thus

$$E_{k_i}(t) = \frac{1}{4}\rho(|v_{x_i}(t)|^2 + |v_{y_i}(t)|^2 + |v_{z_i}(t)|^2). \tag{2}$$
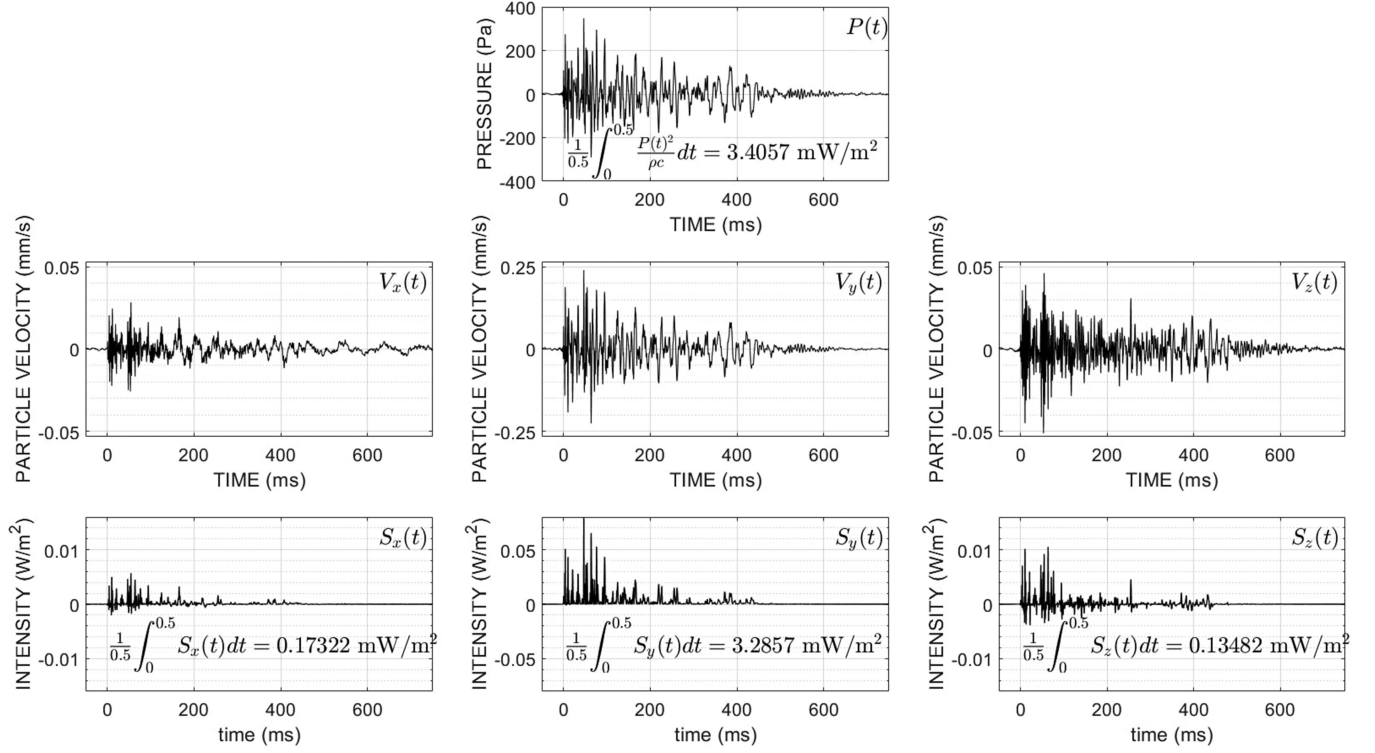
Fig. 5. Top row: Broadband pressure $P(t)$ corresponding to the data in Fig. 4, with time relative to the arrival of the peak waterborne path, also identified is the time average of squared pressure divided by ρc_w. Middle row: Components of broadband particle velocity $V_{x,y,z}(t)$ corresponding to $P(t)$. Note the y-axis for the component V_y ranges from ± 400 Pa when multiplied by ρc_w for ready comparison with $P(t)$. Bottom row: Components of the broadband Umov vector $S_{x,y,z}(t)$ and corresponding time averages.

An image of $E_{k_i}(t)$ [see Fig. 6(b)] closely mirrors $E_{p_i}(t)$, as anticipated from the broadband results (see Fig. 4).

Complex intensity $\vec{I_c}$ as formulated by Heyser [8] is computed as

$$\vec{I_c} = \frac{1}{2} p v^*_{x,y,z} \qquad (3)$$

where the asterisk denotes complex conjugate. Taking the real part of $\vec{I_c}$ yields the active intensity, for which the y-component $I_{y_i}(t)$ is shown in Fig. 6(c); taking the imaginary part yields reactive intensity, where the z- or vertical-component $Q_{z_i}(t)$ is shown in Fig. 6(d) and subscript i denotes a central frequency index for these narrowband quantities. Both $I_{y_i}(t)$ and $Q_{z_i}(t)$ also separate into four modes for frequencies less than about 80 Hz. To emphasize these modal patterns, the data are only plotted where the corresponding $E_{p_i}(t)$ is within 12 dB of the maximum.

Looking ahead, we select and study values of second-order quantities including $I_{y_i}(t)$, $Q_{z_i}(t)$, and others to be defined, that are associated with the time–frequency addresses shown by the dots in Fig. 6(a). For example, a narrowband version of the Umov vector $S_y(t)$ in the y-direction at central frequency $f_i = 45$ Hz [see Fig. 6(e)] is formed by

$$S_{y_i}(t) = \text{Re}\{p_i(t)\}\text{Re}\{v_{y_i}(t)\}. \qquad (4)$$

Active intensity $I_{y_i}(t)$ corresponding to a cut along 45 Hz [see Fig. 6(c), black line] finds support at modes 1, 2, and 3 [see Fig. 6(e)]. We may interpret $I_{y_i}(t)$ as a slowly varying

average value [7], [9] of $S_{y_i}(t)$. More specifically, time integrals of $S_{y_i}(t)$ and $I_{y_i}(t)$ are equal; furthermore, in this narrowband context, $S_{y_i}(t)$ can be approximately reconstructed by multiplying $I_{y_i}(t)$ by $2\cos^2(2\pi f_i t - \phi)$ [10], where ϕ is a phase factor.

Values of $I_{y_i}(t)$ shown by the three black symbols correspond with the time–frequency addresses as extracted from $E_{p_i}(t)$. A similar cut along 30 Hz [see Fig. 6(c), red line] finds support at only modes 1 and 2 given 30 Hz is below the cutoff of mode 3; here, two values of $I_{y_i}(t)$ [see Fig. 6(e), red symbols] correspond with time–frequency addresses.

Vertical reactive intensity $Q_{z_i}(t)$ corresponding to a cut along 45 Hz [see Fig. 6(d), black line] also finds support at modes 1, 2, and 3 [see Fig. 6(f)]. In this case, the vertical component of the Umov vector $S_{z_i}(t)$ time averages to nearly or exactly zero and $Q_{z_i}(t)$ traces the envelope, with $S_{z_i}(t)$ approximately reconstructed by multiplying $Q_{z_i}(t)$ by $\sin(4\pi f_i t - \phi)$ [10]. We observe that for 45 Hz, the envelope $Q_{z_i}(t)$ at the selected values identified by black symbols is negative for modes 1 and 2 and then goes positive for mode 3. (Note: it is the *change* in sign of $Q_{z_i}(t)$ that is important, without physical significance placed on sign [11] other than it be consistent with our time convention of $e^{-i\omega t}$.) A cut along 30 Hz [see Fig. 6(d), red line] finds support at only modes 1 and 2, with the envelope $Q_{z_i}(t)$ shown in Fig. 6(f) along with two selected values identified by the red symbols. In this case, envelope $Q_{z_i}(t)$ for mode 2 is positive. The change in the sign of $Q_{z_i}(t)$ for mode 2 near $\sim$37 Hz is a significant feature of the modal structure as measured at the IVAR location.
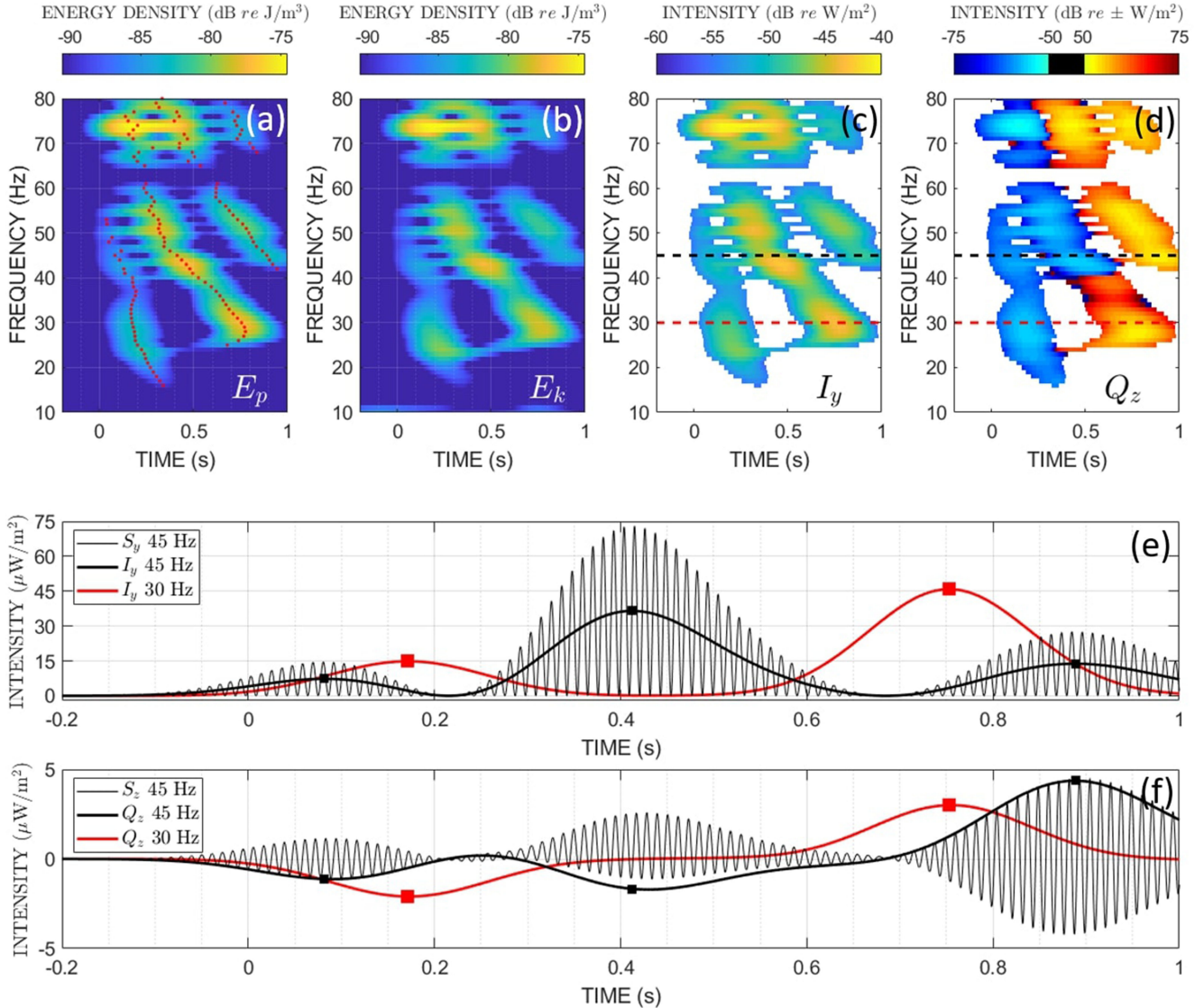
Fig. 6. (a) $E_{p_i}(t)$ measured for one of the five SUS detonations from station S45 (range 10 km). Dots corresponding to maximum values of $E_{p_i}(t)$ identify time–frequency addresses for each mode. (b) Corresponding $E_{k_i}(t)$. (c) and (d) Corresponding $I_{y_i}(t)$ and $Q_{z_i}(t)$ for which thresholding is applied; dashed horizontal lines denote cuts at central frequencies 30 and 45 Hz. (e) Cuts of $I_{y_i}(t)$ along central frequencies 30 Hz (red) and 45 Hz (black) with $S_{y_i}(t)$ centered at 45 Hz also shown for reference. Red and black symbols identify values selected from $I_{y_i}(t)$ to be used in subsequent calculations. (f) Cuts of $Q_{z_i}(t)$ along central frequencies 30 Hz (red) and 45 Hz (black) with $S_{z_i}(t)$ centered at 45 Hz also shown for reference. Red and black symbols identify values selected from $Q_{z_i}(t)$ to be used in subsequent calculations.

IV. FOUR QUANTITIES DERIVED FROM VECTOR ACOUSTIC MEASUREMENTS FOR SINGLE-MODE SINGLE-FREQUENCY AND CORRESPONDING MODELS

The intensity and energy quantities at the individual mode arrivals obtained from the approach outlined in Section III can be combined into four range-independent quantities: phase speed, depth-dependent modal speed of energy, circularity, and normalized vertical reactive intensity. These quantities are sensitive to the geoacoustic properties at the sensor location, and field data from IVAR yield estimates for modes 1–4 and frequencies between about 15 and 80 Hz (with some gaps due to multimode interference near cutoff frequencies). For each quantity, we describe means to obtain a theoretical model developed from a vertical mode function and corresponding horizontal wave

number $k_n(f)$. Any normal mode-based propagation code can be used to obtain these quantities; in our case, we use the Kraken [12] normal mode program (with quantities conjugated as necessary to align with our time convention of $e^{-i\omega t}$).

A. Phase Speed $v_{p_n(f)}$

The phase speed for mode n at frequency f is $v_{p_n(f)}$ and we adapt (27) from Mann et al. [10] to estimate $v_{p_n(f)}$ at discrete frequencies f_i from the data as follows:

$$v_{p_n(f_i)} = \frac{2c_w^2 E_{p_i}(t_n)}{|I|}. \tag{5}$$

Here, $E_{p_i}(t_n)$ denotes a value selected from $E_{p_i}(t)$ at the time–frequency address [see Fig. 6(a)] corresponding with mode n and frequency f_i, and similarly $|I| =$

$\sqrt{I_{x_i}^2(t_n) + I_{y_i}^2(t_n) + I_{z_i}^2(t_n)}$. For example, Fig. 6(e) (red symbols) identifies the selected values of $I_{y_i}(t_n)$ for the first two modes $n = 1, 2$ at $f_i = 30$ Hz. We adapt this notation for other metrics to be defined subsequently as in the corresponding values of $Q_{z_i}(t_n)$ [see Fig. 6(f)].

A model for phase speed is always available from a normal mode-based propagation code. Note the modal phase speed remains a local quantity, relating to the conditions that gave rise to the local mode properties, as distinct from the modal group speed that is a range-integrated quantity [13].

B. Depth-Dependent Mode Speed of Energy $u_{e_n}(z, f)$

D'Spain *et al.* [14] define a velocity of acoustic energy density transport as the ratio of active horizontal intensity to total energy, each expressed as a function of frequency, with the interpretation of this spectral ratio being the speed of net transport of acoustic energy density at the point in space where the measurement is made. The ratio is bounded by the sound speed in the medium c_w. For example, D'Spain *et al.* [14] show that the speed of energy associated with a diffuse background sound field is only about 10%–50% of the medium's sound speed, whereas this speed, when associated with more spatially concentrated sound sources, approaches c_w. This property thus relates to the relative balance between active (concentrated) and reactive (diffuse) fields, with a completely active field reaching a speed c_w and reactive field having a speed equal to 0 [15].

The variable $u_{e_n}(z, f)$ is closely analogous to this definition with the distinction that $u_{e_n}(z, f)$ is designated for individual modes n, and the point in space need only be a function of measurement depth z_m, i.e., the value of $u_{e_n}(z, f)$ does not depend on measurement range. We estimate depth-dependent mode speed of energy from the data using

$$u_{e_n}(z_m, f_i) = \frac{|I_r|}{E_{p_i}(t_n) + E_{k_i}(t_n)} \quad (6)$$

where $|I_r|$ is the magnitude of active intensity in the horizontal direction and equal to $\sqrt{I_{x_i}^2(t_n) + I_{y_i}^2(t_n)}$.

A model for $u_{e_n}(z, f)$ follows from a few variables generated by a mode-based propagation code using local geoacoustic properties and water depth at the measurement site. We start by representing the complex pressure P_n associated with the nth normal mode at range R and receiver depth z as

$$P_n = \frac{e^{ik_n R - i\frac{\pi}{4}}}{\sqrt{k_n R}} U_n(z_s, f) U_n(z, f) \quad (7)$$

where $U_n(z, f)$ is a vertical mode function, z_s is the source depth, and an asymptotic representation for the Hankel function $H_0(k_n R)$ is used. Note that everything to the left of $U_n(z, f)$ in (7) can be represented by a complex constant, call it A_n. Continuing with the single-mode single-frequency representation, the corresponding horizontal particle velocity V_{r_n} is

$$V_{r_n} = A_n k_n U_n(z, f)/(2\pi f \rho) \quad (8)$$

where a second term in V_{r_n} associated with the horizontal derivative becomes negligible compared with the first term for ranges greater than a few wavelengths and is thus ignored here. The corresponding vertical particle velocity V_{z_n} is

$$V_{z_n} = A_n i \frac{dU_n(z, f)}{dz}/(2\pi f \rho). \quad (9)$$

Henceforth, let the abbreviations P_n, V_{r_n}, and V_{z_n} stand for complex pressure, horizontal velocity, and vertical particle velocity, respectively, for mode n, with each being a function of depth and frequency.

The model for depth-dependent mode speed of energy is thus

$$u_{e_n}(z, f) = \frac{\text{Re}\{P_n V_{r_n}^*\}}{0.5|P_n|^2/(\rho c_w^2) + 0.5\rho(|V_{r_n}|^2 + |V_{z_n}|^2)} \quad (10)$$

where the numerator is represented by single-mode depth-dependent horizontal flux and the denominator is composed of single-mode depth-dependent potential and kinetic energy densities.[3]

We remark that the single-mode vertical flux $\text{Re}\{P_n V_{z_n}^*\}$ equals 0, though for simultaneous arrivals of two or more modes at the same frequency, there can be nonzero vertical flux. This interesting effect is under study but is beyond the scope of this paper. Furthermore, in evaluating the model associated with a single mode, the factor A_n is common to both the numerator and denominator and thus cancels. Therefore, the range R along with cylindrical spreading does not enter into the model result. The three models to be defined below also share this property.

It is tempting to interpret $u_{e_n}(z, f)$ as a modal group speed. However, if we evaluate the quantities in (10) for all depths and take the depth integrals of the numerator and denominator separately, we arrive precisely at the group speed for mode n and frequency f as shown by Tolstoy [16]. In that work, $2E_k$ is used instead of $E_p + E_k$, which is a statement of Rayleigh's principle [17], where integrals over the depth of the kinetic and potential energy densities are equal. Nonetheless, given our measurements are at a single depth, we show that $u_{e_n}(z, f)$ differs greatly from a modal group speed even though it displays a high degree of sensitivity to changes in geoacoustic parameters.

C. Circularity $\theta_n(z, f)$

The phase and amplitude difference in orthogonal components of the particle velocity determines the trajectory of particle motion. For example, if at some position in the field, narrowband horizontal and vertical particle velocities are of equal amplitude and 90° out of phase, the result is a perfectly circular trajectory. The other extreme is when particle velocity exists as a single component, as in single plane wave, producing a trajectory along a line. In between these two extremes, the trajectory can be elliptical [18].

The trajectory pattern is described by the variable circularity θ, which ranges from ± 1 (circular, with sign defining rotational direction) to 0 (trajectory along a line). In general, circularity is a vector with $x, y,$ and z components describing the trajectory of particle motion projected onto the $y - z$, $x - z$, and

---

[3]Factors of 1/2 in (1) and (2) are absent here as these manipulations do not involve a Hilbert transform.

$x - y$ planes, respectively, computed using the normalized vector product of complex-valued particle velocity $\vec{v}$ [19], as in

$$\vec{\theta} = \frac{\text{Im}\{\vec{v} \times \vec{v}^*\}}{|\vec{v}|}. \tag{11}$$

Circularity may also be interpreted as the normalized curl of active intensity [20].

For many geometries describing an underwater waveguide, it is both practical and realistic to discuss circularity as a scalar metric with horizontal and vertical particle velocities establishing particle trajectory in the range–depth ($r - z$) plane. For example, such a trajectory is readily observed with a vector sensor lowered through an acoustic field simulating a Lloyd's mirror condition [22]. Measurements of scalar circularity θ as it evolves with a varying source depth that produced a change in multipath interference structure have also been used in geoacoustic inversion [19].

In this paper, we use scalar circularity defined as a function of mode number, measurement depth, and frequency, calling it $\theta_n(z, f)$. However, for our field observations, it is first necessary to project the measurements of $v_{x_i}(t)$ and $v_{y_i}(t)$ (each being complex) into a single horizontal particle velocity v_{r_i} using

$$v_{r_i} = v_{x_i} \cos(\phi_B - \phi_x) + v_{y_i} \cos(\phi_B - \phi_y) \tag{12}$$

where ϕ_x is the bearing of x channel, ϕ_y is the bearing of y channel, and ϕ_B is the bearing of IVAR from a particular SUS station. Knowing $v_{r_i}(t)$ and $v_{z_i}(t)$, the equation to estimate scalar circularity from field data reduces to

$$\theta_n(z_m, f_i) = \frac{2\,\text{Im}\{v_{r_i}(t_n)v_{z_i}^*(t_n)\}}{|v_{r_i}(t_n)|^2 + |v_{z_i}(t_n)|^2}. \tag{13}$$

A model for $\theta_n(z, f)$ emerges by using previously derived model values for V_{r_n} and V_{z_n} as follows:

$$\theta_n(z, f) = \frac{2\,\text{Im}\{V_{r_n} V_{z_n}^*\}}{|V_{r_n}|^2 + |V_{z_n}|^2}. \tag{14}$$

D. Normalized Vertical Reactive Intensity $Q_{z_n}^\star(z, f)$

The vertical component of reactive intensity was introduced [see Fig. 6(d)]. D'Spain et al. [14] explain the significance of vector quantity $\vec{Q}$ by multiplying the equation for conservation of momentum by pressure and then operating in the spectral domain. It is useful to provide here a small variation on this development; keeping in the time domain and using the Hilbert transformed variables (see Section III) yields

$$i2\pi f\rho\, p\vec{v}^* + p\nabla p^* = 0. \tag{15}$$

Assuming a spatial dependence in p going as $|p(x, y, z))| e^{i\phi(x,y,z)}$ gives

$$\pi f\rho\vec{Q} + i\pi f\rho\vec{I} + |p|\nabla|p| + i|p|^2\nabla\phi = 0 \tag{16}$$

and after equating real and imaginary parts and dividing by $|p|^2$, we obtain the desired result as

$$\rho c_w \frac{\vec{Q}}{|p|^2} = \frac{\nabla|p|^2\lambda}{4\pi|p|^2} \tag{17}$$

with the interpretation that reactive intensity normalized by a scalar intensity gives the fractional change of field magnitude squared per unit wavelength [14].

Normalizing reactive intensity $\vec{Q}$ by a scalar intensity ($|p|^2/\rho c_w$) removes the range dependence and provides advantages because important properties emerge in regions of low signal level (see the research work by Dall'Osto et al. [21]). We refer to this normalized quantity as $\vec{Q}^\star$ (where the star symbol identifies this as a normalized quantity and should not be confused with the complex conjugation.) The immediate focus in this paper is on the vertical component of $\vec{Q}^\star$, which, as in the above metrics, is defined here as the function of mode number, measurement depth, and frequency, or $Q_{z_n}^\star(z, f)$. From field data, we estimate $Q_{z_n}^\star(z, f)$ as

$$Q_{z_n}^\star(z_m, f_i) = \rho c_w \frac{Q_{z_i}(t_n)}{|p_i(t_n)|^2} \tag{18}$$

and a model for $Q_z^\star(z, f)$ using the previously derived single-mode pressure and particle velocity as a function of frequency is

$$Q_{z_n}^\star(z, f) = \rho c_w \frac{\text{Im}\{P_n V_{z_n}^*\}}{|P_n|^2}. \tag{19}$$

Note the behavior of $Q_{z_n}^\star(z_m, f_i)$ and $\theta_n(z_m, f_i)$ and corresponding models will be similar, as anticipated from the numerators of (14) and (19), both of which govern the sign change. That is, given that the radial particle velocity $v_{r_i(t)}$ and pressure $p_i(t)$ are likely to be nearly exactly in phase for the active field then $Q_{z_n}^\star(z_m, f_i)$, which is based on the latter, will have similar behavior. However, each provides an independent examination of the data, because the denominator of $\theta_n(z_m, f_i)$ includes both horizontal and vertical components of particle velocity and this quantity is bound by ± 1, whereas that of $Q_{z_n}^\star(z_m, f_i)$ is based on pressure and can assume extreme values, especially when evaluated near complicated multimode interference structures [21].

E. Comparison of Model Results Based on Two Geoacoustic Models

Model results for the four quantities derived from the vector acoustic measurements are compared using two different geoacoustic representations (or geoacoustic models), the first being a notional one for the SBCEX experimental conditions corresponding to the IVAR location and the second being a half-space, or Pekeris representation (see Table I). We emphasize that the notional geoacoustic model is not a result of an inversion per se but instead meant as a nominally consistent representation of available ground truth data in terms of water depth measured at IVAR (mean depth, 74.4 m), measured water sound speed c_w, and approximate mud-layer thickness at the IVAR site based high-resolution chirp acoustic reflection data [1]. Some experimentation with forward modeling is required to establish parameters for the mud layer, a key component of the notional geoacoustic model, and we use values consistent with those emerging from recently published studies [2], [4], such as mud-layer thickness and linear sound-speed gradient equal to $10\,\text{s}^{-1}$.

TABLE I
SUMMARY OF GEOACOUSTIC REPRESENTATIONS

Notional SBCEX	Layer Thickness	Sound Speed	Density	Attenuation
Water	74.4 m	1468.3 m/s	1027 kg/m^3	0 dB/λ
Mud	11 m	1445-1555 m/s	1600 kg/m^3	0.05 dB/λ
Halfspace	semi-infinite	1830 m/s	2000 kg/m^3	0.25 dB/λ
Pekeris	Layer Thickness	Sound Speed	Density	Attenuation
Water	74.4 m	1468.3 m/s	1027 kg/m^3	0 dB/λ
Halfspace	semi-infinite	1830 m/s	2000 kg/m^3	0.25 dB/λ

We first undertake a brief analysis of sediment attenuation to confirm that the attenuation parameters (see Table I) are at least nominally consistent with the data. For a given source station, active horizontal intensity for modes $n = 1, 2, 3$ and frequency indices f_i between about 15 and 60 Hz (depending on mode) is taken to be $\sqrt{I_{x_i}^2(t_n) + I_{y_i}^2(t_n)}$. For example, for the SUS station S45 at range 10 km [see Fig. 6(e)], active horizontal intensity is dominated by the y-component and $I_{y_i}(t_n)$ at 30 Hz for modes 1 and 2 are 0.05 and 0.13 mW/m^2, respectively.

Data from all stations studied (see Fig. 3) are collected in this manner, and we assume these data take on a range behavior embodied by $|A_n|^2$, which will have the range dependence going as $e^{-2\text{Im}\{k_n\}R}/R$. The cylindrical spreading term is removed, and what remains is the decay for a particular mode governed by the imaginary part of the modal horizontal wave number $k_n(f_i)$. For example, the entire set of active horizontal intensity data for mode 2, 30 Hz (see Fig. 7 inset) is fitted to a single curve, with cylindrical spreading built in, and an estimate of $\text{Im}\{k_n(f_i)\}$ is then derived from this curve fit (solid line in Fig. 7 inset). Results for the first three modes (see Fig. 7) show that the imaginary part of the horizontal wave number increases rapidly near the cutoff of the mode, and then assumes a more constant value. Admittedly, this is a delicate operation on the data with results susceptible to interference effects. Nonetheless, the analysis confirms that $\text{Im}\{k_n\}$ values derived from the notional SBCEX geoacoustic model based on less attenuation in the mud layer than in the sediment half-space (see Fig. 7, solid, black lines) are reasonably consistent.

More detail is required to describe sediment attenuation properly. For now, we accept this deficiency in our notional SBCEX geoacoustic model given its purpose in this paper, with the results (see Fig. 7) motivating a more refined inversion on sediment attenuation. Finally, we note that this analysis can also be undertaken using potential energy $E_{p_i}(t_n)$ measured as a function of range based on a single pressure sensor (thick, dotted lines in Fig. 7). These results are in agreement with those derived from active horizontal intensity with the exception of mode 1, which covers a much lower frequency range. Here signal-to-noise limitations that affect the pressure and velocity channels differently can be an issue.

Based on the geoacoustic data in Table I, we compute, as a function of frequency for modes 1–4, model results (see Fig. 8) for depth-dependent mode speed of energy $u_{e_n}(z, f)$ (10), circularity $\theta_n(z, f)$ (14), and normalized vertical reactive intensity $Q_{z_n}^\star(z, f)$ (19). Also coming directly from the normal mode calculations are phase speed $v_{p_n(f)}$ and group speed $v_{g_n(f)}$, for which the latter, although not included in the four quantities to be derived from the vector acoustic measurements, will be interesting to include.

The different behaviors for $u_{e_n}(z, f)$, $\theta_n(z, f)$, and $Q_{z_n}^\star(z, f)$ based on notional SBCEX and Pekeris models are striking, and suggests that these quantities, when in the form of reliable field data, have great potential to resolve information about the seabed. When based on the notional SBCEX model, both $\theta_n(z, f)$ and $Q_{z_n}^\star(z, f)$ also undergo a change in sign for mode 2 at 37 Hz, whereas when based on the Pekeris model, the sign change for mode 2 occurs very close to, if not precisely at, the cutoff frequency for mode 2, which is approximately 25 Hz. In terms of the parameters given in Table I, the mud-layer thickness combined with the average compressional wave speed within this layer appears to have the greatest controlling influence on this property.

V. RESULTS

Experimental values (see Fig. 9) are presented for the mode- and frequency-dependent vector acoustic quantities (see Sections IV-A–IV-D) , based on observations from 22 SUS stations (see Fig. 3) for which the range to IVAR exceeds 5 km and there is sufficient dispersion to identify separate mode arrivals (see Fig. 6(a)]. Additionally, the modal group speed $v_{g_n}(f_i)$ is estimated directly from the time–frequency address locations generated from E_p for any arrival [see Fig. 6(a)]. Given the known range R between SUS detonation and IVAR and water sound speed c_w, $v_{g_n}(f_i) = R/t$, where $t = t_0 + \Delta t$ is the total travel time, with Δt established by the time–frequency address and $t_0 = R/c_w$ is the arrival time of the broadband peak.

Each quantity has 110 independent estimates, based on the five SUS detonations for a given station (range) and 22 stations used in this analysis. As a measure of central tendency and to avoid undue influence of outliers, we use the median value
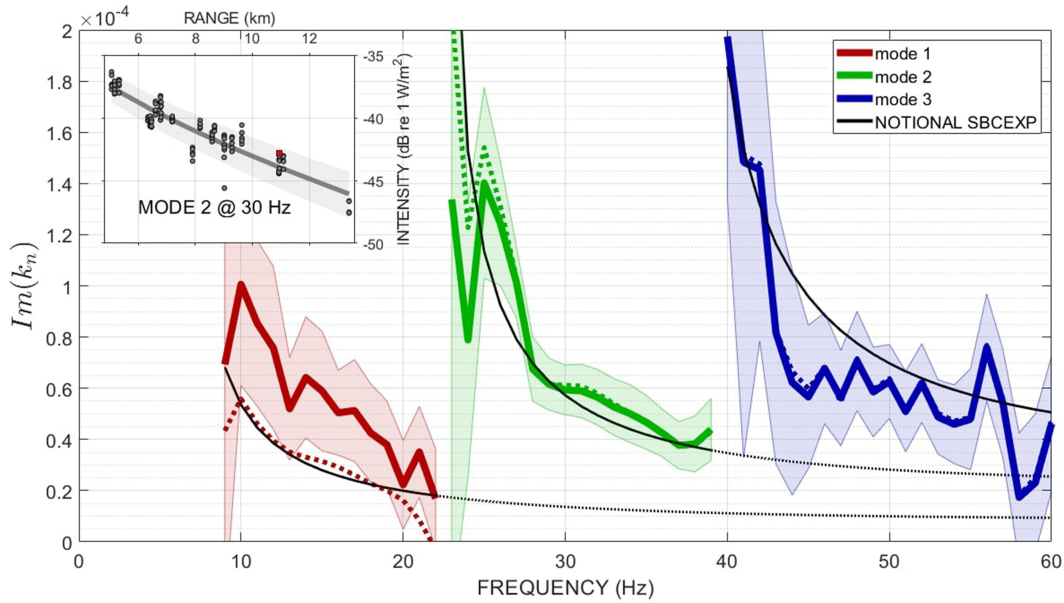
Fig. 7. Imaginary part of horizontal wave number k_n for modes $n = 1, 2, 3$ as derived from analysis of horizontal intensity from SUS arrivals measured at the IVAR site, ranges 5–13 km. Thicker color-coded solid lines represent the median estimate of $\text{Im}\{k_n\}$ as a function of central frequency f_i, with shading bracketing the 95th percentile range. Color-coded dotted lines are equivalent estimates based on potential energy (see text) that align with those based on horizontal intensity with exception of mode 1. Solid, black lines are values $\text{Im}\{k_n\}$ from the Kraken normal mode program upon using the attenuation values in Table I. Inset: Example of active horizontal intensity as function of range for mode 2 and central frequency 30 Hz. Thick line is fitted curve from which estimates of $\text{Im}\{k_n\}$ are derived.
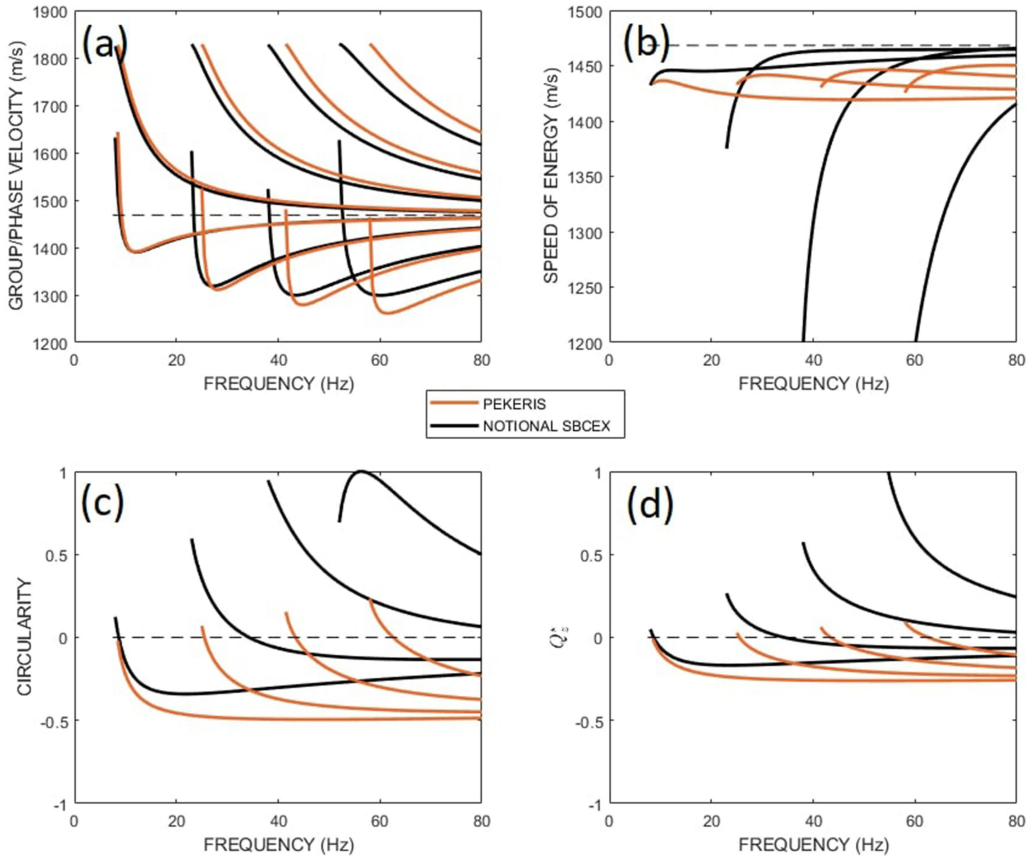

Fig. 8. Theoretical predictions for the four vector acoustic quantities plus group speed, based on the two geoacoustic models in Table I. (a) Phase speed $v_{p_n}(f)$ (above the horizontal dashed line c_w) and corresponding group speed $v_{g_n}(f)$. (b)–(d) Depth-dependent vector acoustic quantities evaluated at IVAR depth: (b) mode speed of energy $u_{e_n}(z, f)$ with horizontal dashed line equal to c_w, (c) scalar circularity $\theta_n(z, f)$, and (d) vertical component of reactive intensity normalized by scalar intensity $Q^\star_{z_n}(z, f)$
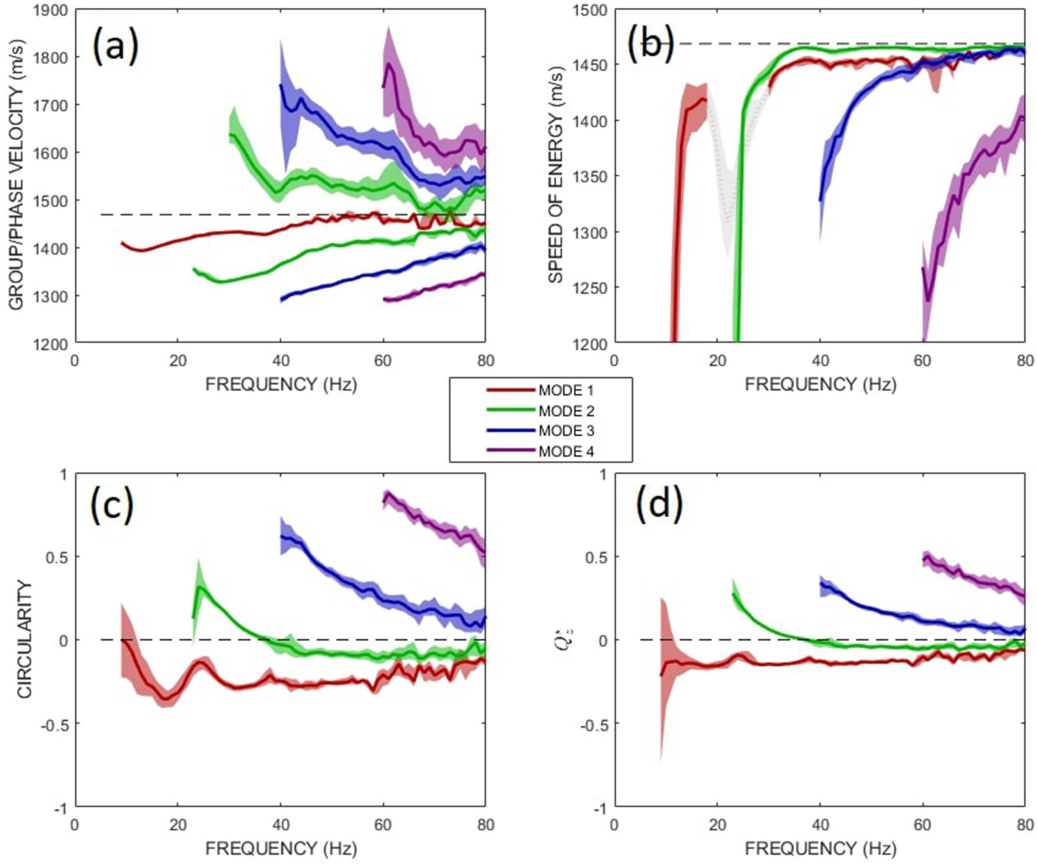
Fig. 9. (a) Experimental values of phase speed $v_{p_n}(f_i)$ (above the horizontal dashed line) and group speed $v_{g_n}(f_i)$ (below the dashed line). (b) Mode speed of energy $u_{e_n}(z_m, f_i)$. (c) Scalar circularity $\theta_n(z_m, f_i)$. (d) Vertical component of reactive intensity normalized by scalar intensity $Q^\star_{z_n}(z_m, f_i)$.

as the final estimate (thick lines in Fig. 9) with uncertainty characterized by the 25th (lower bound) and 75th percentiles.

Group speed estimates based on the pressure channel [see Fig. 9(a)] suggest a frequency of the Airy phase for mode 2 at 28 Hz, which is in agreement with that recently reported by Wan *et al.* [4]; additionally, we report an Airy phase group speed for mode 2 equal to 1328 m/s (median), with a 25th–75th percentile range of 1326–1333 m/s. However, signal-to-noise limitations prevented estimates of the Airy phase for modes 3 and 4. The Airy phase of mode 1 has a frequency of 13 Hz and speed 1393 m/s with 25th–75th percentile equal to 1392–1396 m/s. The estimates of group speed are from varying angular sectors (see Fig. 3) and thus necessarily represent a range average over differing mud thicknesses [1], see also [4, Fig. 1], yet the bounds on these estimates are reasonably tight. This observation is anticipated based on the results from the notional geoacoustic model [see Fig. 8(a)], for which group velocities (black lines) are consistent with our experimental values for mode 1 and mode 2; however, these results are expected to shift little by changing the mud-layer thickness a meter or two because the Pekeris model yields similar results.

For estimates of phase speed $v_{p_n(f)}$ [estimates located above the dashed line equal to c_w in Fig. 9(a)], variation about the median for any given frequency is greater and a reliable estimate of mode 1 phase speed is not possible, although the phase speed estimates obtained are reasonably comparable with those from

the notional geoacoustic model [see Fig. 8(a)]. As with group speed, model estimates of phase speed also show considerable similarity between the two widely different geoacoustic models, particularly for modes 1 and 2, and we anticipate that these observations offer a lower measure of information about the seabed.

The three quantities relating to individual-mode frequency-dependent estimates of the mode speed of energy [see Fig. 9(b)], circularity [see Fig. 9(c)], and normalized vertical reactive intensity [see Fig. 9(d)], all of which are depth dependent, present an interesting collective case. Inspecting their patterns versus frequency and mode number suggests that there is information in these data that motivates resolving more than a half-space, or Pekeris, representation for a geoacoustic model, and that something like the notional geoacoustic model (see Table I) is required. At this point, we postpone a formal geoacoustic inversion to future work or to works by other researchers studying these data.

However, a key property of mode 2 as observed at the IVAR location is the zero crossing near 37 Hz for estimates of $\theta_n(z_m, f_i)$ [see Fig. 9(c)] and $Q^\star_{z_n}(z_m, f_i)$ [see Fig. 9(d)]; any geoacoustic model that originates from this experiment ought to exhibit this property in mode 2 when applied to the IVAR location (depth 74.4 m). Thus, we posit this value as a constraint observation for mode 2, with formal median value of 37.3 Hz and 25th–75th percentile range of 36–39 Hz.
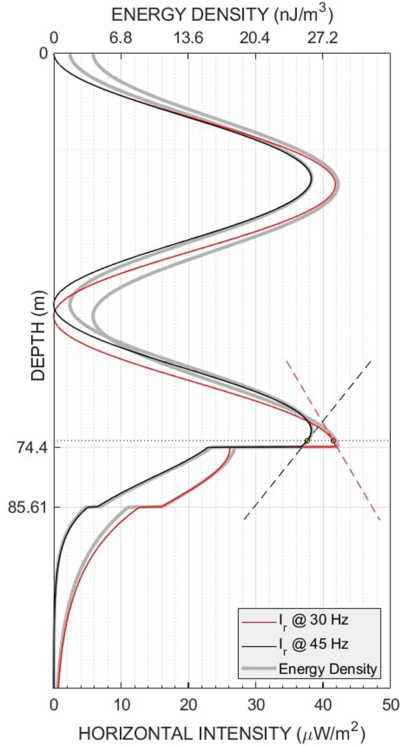
Fig. 10.   Horizontal intensity for mode 2 at 30 Hz (red) and 45 Hz (black) assuming the notional SBCEX geoacoustic model (see Table I) combined with true measurements made at the IVAR measurement depth (horizontal dotted line). Energy densities (thick gray lines) follow closely the corresponding horizontal intensities as seen by the overlapping lines, which separate toward the sea surface. Two slope indicators (short, dashed lines) indicate the sign of the vertical derivative of the pressure magnitude squared at the IVAR measurement depth.

To further understand this property, we examine the behavior of mode 2 at two frequencies that span 37 Hz (see Fig. 10) based on the notional SBCEX geoacoustic model (see Table I). Take for purposes of demonstration, values for energy density $E_{p_i}(t_n) + E_{k_i}(t_n)$ and horizontal intensity $\sqrt{I_{x_i}^2(t_n) + I_{y_i}^2(t_n)}$ observed at the IVAR measurement depth z_m for mode 2 at 30 Hz and 45 Hz, as can be inferred from Fig. 6(a)–(c), noting in this case $I_{x_i}(t_n) \approx 0$. Using the notional SBCEX geoacoustic model, we compute $U_n(z)$ and k_n for $n = 2$ at 30 and 45 Hz and derive an estimate of $|A_n|^2$ for $n = 2$ at these frequencies by equating the measured to theoretical values of horizontal intensity I_r, where

$$I_r = \frac{|A_n|^2 \mathrm{Re}\{k_n\} |U_n(z)|^2}{2\pi f \rho(z)}. \tag{20}$$

Using (20), I_r may now be extrapolated over the entire water column and sediment depth where we require a depth-dependent density $\rho(z)$. An analogous operation is applied to energy density, with both I_r and $E_p + E_k$ as functions of depth shown for mode 2 at frequencies 30 and 45 Hz (see Fig. 10).

Returning to the original issue of the zero crossing, take I_r as surrogate for $|p|^2$ as used in (17) to demonstrate how reactive intensity relates to the gradient of the pressure magnitude squared. The vertical derivative of I_r changes sign at the IVAR measurement depth between frequencies 30 and 45 Hz

(see slope indicators, Fig. 10) and equals 0 at approximately 37 Hz, which explains the behavior in $Q_{z_n}^\star(z_m, f_i)$. Similarly, on a single-mode basis, pressure and horizontal particle velocity are in phase, and therefore estimates of scalar circularity behave like $Q_{z_n}^\star(z_m, f_i)$ in terms of the sign change property for mode 2. (Observe that I_r can be discontinuous across the water–sediment boundary, whereas I_z will be continuous [23].)

Estimates for the modal speed of energy [see Fig. 9(b)], which assume seemingly nonintuitive values [i.e., resembling nothing like the phase or group speeds shown in Figs. 8(a) and 9(a)], mirror the estimates based on the notional SBCEX model [see Fig. 8(b)]. Over frequencies 30–45 Hz, estimates for the speed of energy for mode 2 vary smoothly from ∼1442 m/s to ∼1465 m/s, which is slightly less than the c_w value and there are similar changes observed for modes 1, 3, and 4 but over different frequency ranges.

VI. SUMMARY AND ADDITIONAL REMARKS

The IVAR is a system that records four coherent channels of acoustic data continuously: one channel for acoustic pressure and three channels associated with a triaxial accelerometer from which acoustic particle velocity is obtained. Using the IVAR, the vector acoustic field of broadband signals originating from SUS (Mk-64) charges deployed at ranges 5–13 km from the fixed IVAR site (mean depth 74.4 m) were studied as part of the 2017 SBCEX relating to the study of the acoustics of fine-grained muddy sediments. Sufficient geometric dispersion at these ranges permitted unambiguous identification of up to four modes as a function of frequency in the range ∼15–80 Hz.

From the time–frequency analysis of the dispersed arrivals, time–frequency addresses of single-mode (n) and single-frequency (f_i) arrivals are identified. Four vector acoustic quantities are estimated at each address: first, mode phase speed $v_{p_n}(f_i)$; second, depth-dependent mode speed of energy $u_{e_n}(z_m, f_i)$; third, scalar circularity $\theta_n(z_m, f_i)$; and fourth, normalized vertical reactive intensity $Q_{z_n}^\star(z_m, f_i)$, for which the last three depend on the IVAR measurement depth z_m of 1.25 above the seafloor. In addition, modal group speed $v_{g_n(f_i)}$ is estimated directly from the dispersed arrivals measured on the pressure channel.

A comprehensive feature of these observations, measured at ranges 5–13 km, is the general collapse onto a single curve as a function of frequency for a given mode, although some better than others. This implies that these data represent a measure of the local mode properties as realized at the IVAR site; the observations of group speed are an exception in that they represent an average group speed for the SBCEX experimental area at the particular measurement range [2].

The observations are easily modeled using a normal mode-based propagation code providing a pathway for geoacoustic inversion. A comparison of observations with model results, with the latter based on: first, a notional geoacoustic representation for the SBCEX experimental area consisting of single low-speed mud layer over a half-space, and second, a Pekeris representation based on the same half-space (see Table I), shows striking differences (see Fig. 8). The field observations (see Fig. 9) are clearly at variance with the Pekeris representation. The notional

geoacoustic representation is designed to be consistent with available ground truth and incorporate sediment attenuation parameters based on experimental results on the range decay of identifiable mode arrivals to estimate $\text{Im}\{k_n\}$. Beyond this, a formal inversion to assess more quantitatively the resolving power of these data, for example, the ability to resolve sound-speed gradients, or additional granularity in sediment layering, requires further study.

Nonetheless, the notional geoacoustic representation for the SBCEX experimental area does provide some guidance. In particular, mode properties emerging from it predict well the zero crossing near 37 Hz for mode circularity [see Fig. 8(c)] and normalized vertical reactive intensity [see Fig. 8(d)]. This effect is manifested in observations of $\theta_n(z_m, f_i)$ and $Q_{z_n}^\star(z_m, f_i)$ in the form of a zero crossing and change in sign, a property that is observed consistently in more than 100 observations based on the 5–13 km source range set. It is a fundamental feature of the mode structure as realized at the IVAR site that cannot be reproduced in the absence of a low-speed, mudlike layer.

Finally, although it is demonstrated that information content in $u_{e_n}(z_m, f_i)$, $\theta_n(z_m, f_i)$, and $Q_{z_n}^\star(z_m, f_i)$ as data measures for geoacoustic inversion appears to be high, they are not sensitive to sediment attenuation. Note that this insensitivity is a feature of the single-mode representation of these quantities, and then for a field subject to multimode interference, range dependence and sensitivity to attenuation likely would be exhibited. However, our analysis of active horizontal intensity as a function of mode and frequency for all ranges to obtain estimates of $\text{Im}\{k_n\}$ suggests that much less attenuation in the mud layer than in the sediment half-space (see Table I) is required to be compatible with observations. It is possible that other vector acoustic quantities, such as active vertical intensity or reactive horizontal intensity, will be of greater use as a measure of sediment attenuation, and furthermore not require observations over range. This, too, will be assessed in future work.

ACKNOWLEDGMENT

REFERENCES

[1] J. A. Goff, A. H. Reed, G. Gawarkiewicz, P. S. Wilson, and D. P. Knobles, "Stratigraphic analysis of a sediment pond within the New England Mud Patch: New constraints from high-resolution chirp acoustic reflection data," *Mar. Geol.*, to be published.

[2] J. Bonnel *et al.*, "Geoacoustic inversion on the New England Mud Patch using warping and dispersion curves of higher-order modes," *J. Acoust. Soc. Amer.*, vol. 143, pp. EL405–EL411, 2018.

[3] C. B. Leslie, J. M. Kendall, and J. L. Jones, "Hydrophone for measuring particle velocity," *J. Acoust. Soc. Amer.*, vol. 28, pp. 711–715, 1956.

[4] L. Wan, M. Badiey, D. P. Knobles, and P. S. Wilson, "The airy phase of explosive sounds in shallow water," *J. Acoust. Soc. Amer.*, vol. 143, pp. EL199–EL205, 2018.

[5] L. M. Brekhovskikh, *Waves in Layered Media*. New York, NY, USA: Academic Press, 1960.

[6] N. R. Chapman, "Measurement of the waveform parameters of shallow explosive charges," *J. Acoust. Soc. Amer.*, vol. 78, pp. 672–681, 1985.

[7] F. J. Fahy, *Sound Intensity*, 2nd ed. London, U.K.: Chapman & Hall, 1995.

[8] R. C. Heyser, "Instantaneous intensity," in *Proc. 81st Conv. Audio Eng. Soc.*, Los Angeles, CA, USA, Nov. 12-16, 1986, Art. no 2399.

[9] F. Jacobsen, "A note on instantaneous and time-averaged active and reactive intensity," *J. Sound Vib.*, vol. 147, pp. 489–496, 1991.

[10] J. A. Mann III, J. Tichy, and A. J. Romano, "Instantaneous and time averaged energy transfer in acoustic fields," *J. Acoust. Soc. Amer.*, vol. 82, pp. 17–30, 1987.

[11] F. Jacobsen, "Active and reactive, coherent an incoherent sound fields," *J. Sound Vib.*, vol. 130, no. 3, pp. 493–507, 1989.

[12] M. B. Porter and E. L. Reiss, "A numerical method for ocean acoustic normal modes," *J. Acoust. Soc. Amer.*, vol. 76, pp. 244–252, 1984.

[13] F. B. Jensen, W. A. Kuperman, M. B. Porter, and H. Schmidt, *Computational Ocean Acoustics*, 2nd ed. New York, NY, USA: Springer, 2011.

[14] G. L. D'Spain, W. S. Hodgkiss, and G. L. Edmonds, "Energetics of the deep oceans infrasonic sound field," *J. Acoust. Soc. Amer.*, vol. 89, pp. 1134–1158, 1991.

[15] G. Schiffrer and D. Stanzial, "Energetic properties of acoustic fields," *J. Acoust. Soc. Amer.*, vol. 96, pp. 3645–3653, 1994.

[16] I. Tolstoy, "Resonant frequencies and high modes in layered waveguides," *J. Acoust. Soc. Amer.*, vol. 28, pp. 1182–1192, 1956.

[17] A. Pierce, "The natural reference wavenumber for parabolic approximations in ocean acoustics," *Comput. Math. Appl.*, vol. 11, pp. 831–841, 1985.

[18] V. A. Shchurov, *Vector Acoustics of the Ocean*. Vladivostok, Russia: Dalnauka, 2006.

[19] D. R. Dall'Osto, J. W Choi, and P. H. Dahl, "Measurement of acoustic particle motion in shallow water and its application to geoacoustic inversion," *J. Acoust. Soc. Amer.*, vol. 139, pp. 311–319, 2016.

[20] D. R. Dall'Osto and P. H. Dahl, "Observations of water column and bathymetric effects on the incident acoustic field associated with shallow water reverberation experiments," *IEEE J. Ocean. Eng.*, vol. 42, no. 4, pp. 1146–1161, Oct. 2017.

[21] D. R. Dall'Osto, P. H. Dahl, and J. W. Choi, "Properties of the acoustic intensity vector field in a shallow water waveguide," *J. Acoust. Soc. Amer.*, vol. 131, pp. 2023–2035, 2012.

[22] D. R. Dall'Osto and P. H. Dahl, "Elliptical particle motion in underwater waveguides," *J. Acoust. Soc. Amer.*, vol. 134, pp. 109–118, 2013.

[23] D. M. F. Chapman, "Using streamlines to visualize acoustic energy flow across boundaries," *J. Acoust. Soc. Amer.*, vol. 124, pp. 48–56, 2008.

Peter H. Dahl (M'02–SM'17) received the Ph.D. degree in ocean engineering from the Massachusetts Institute of Technology, Cambridge, MA, USA/Woods Hole Oceanographic Institution, Woods Hole, MA, USA, Joint Program in Oceanography and Oceanographic Engineering, in 1989.

He is currently a Senior Principal Engineer with the Applied Physics Laboratory, University of Washington, Seattle, WA, USA, and a Professor in mechanical engineering with the University of Washington. His research interests include experimental and modeling studies on intensity vector acoustics, the influence of sea surface conditions on underwater sound propagation and reverberation, and studies on the underwater sound field from pile driving and explosive sources.

Dr. Dahl is a Fellow of the Acoustical Society of America (ASA). He was the Chair for the ASA Technical Committee on Underwater Acoustics and the ASA Executive Council and the ASA Vice-President (2013–2014.) He was a Chief Scientist on *R/V Endeavor* (Leg 1) during the Office of Naval Research Seabed Characterization Experiment.

David R. Dall'Osto received the Ph.D. degree in mechanical engineering from the University of Washington, Seattle, WA, USA, in 2013.

He is currently a Senior Research Scientist and Engineer with the Applied Physics Laboratory, University of Washington. His research interests include modeling and measurement of acoustic intensity in the ocean and atmosphere, on both short-range and global scales. An important aspect of his research is the discovery of physical processes that produce structure in the intensity vector field and validating such theoretical predictions through experiment.